Experimentally finding dense subgraphs using a time-bin encoded Gaussian boson sampling device

S. Sempere-Llagostera,[1] R. B. Patel,[1,2] I. A. Walmsley,[1] and W. S. Kolthammer[1]

[1] *Department of Physics, Imperial College London, Prince Consort Rd, London SW7 2AZ, UK*
[2] *Clarendon Laboratory, University of Oxford, Parks Road, Oxford, OX1 3PU, UK*

(Dated: April 12, 2022)

Gaussian Boson Sampling (GBS) is a quantum computing concept based on drawing samples from a multimode nonclassical Gaussian state using photon-number resolving detectors. It was initially posed as a near-term approach aiming to achieve quantum advantage, but several applications have been proposed ever since, such as the calculation of graph features or molecular vibronic spectra, among others. For the first time, we use a time-bin encoded interferometer to implement GBS experimentally and extract samples to enhance the search for dense subgraphs in a graph. Our results indicate an improvement over classical methods for subgraphs of sizes three and four in a graph containing ten nodes. In addition, we numerically explore the role of imperfections in the optical circuit and on the performance of the algorithm.

I. INTRODUCTION

Quantum computing promises to modify the current computational paradigm [1, 2] by providing a substantial speedup in the computation of specific tasks that are currently intractable. Two key milestones have been achieved in the field so far; (i) theoretically developing algorithms that show a quantum speedup compared to the classical counterpart [3], and, (ii) experimentally implementing some protocol that exhibits a quantum advantage, i.e. that are not possible to simulate in a classical computer [4, 5]. Now, meeting these two at a common ground where we show a *practical* quantum advantage is the next necessary step. Two main avenues exist to achieve this, either by building a fault-tolerant universal quantum computer or by coming up with devices that can outperform the classical method in a specific task conceived as useful. Despite consistent progress over the last few years, the former still seems a bit far away in time, while the latter exhibits promising prospects in the near term for particular scenarios [6].

In the optical domain, Gaussian Boson Sampling [7, 8] has emerged as a potential candidate in this regard. GBS involves injecting a multimode nonclassical Gaussian state into an interferometer and measuring the number of photons at each output. The classical procedure to simulate this sampling problem requires the computation of a mathematical function called the Hafnian. Calculating the Hafnian constitutes a #P-hard problem, meaning it is not efficiently computable on a classical computer [7, 9]. So far, GBS has found applications both as a smaller part in the bigger quantum computer picture as a resource state generator [10, 11], and as a standalone device that can be used, for instance, to calculate vibronic spectra of molecules or graph features [12–14]. Concerning the two key milestones referred to previously, a quantum advantage has been achieved by means of a GBS experiment [5, 15], but no practical application has been demonstrated yet. However, in a recent paper, Arrazola et al. [16] showed promising results on this avenue.

A key challenge of optical interferometers is to scale them up in the number of modes. Traditionally, the information carried by an optical state is encoded in its polarisation or spatial modes, implying the need for extensive hardware requirements when scaling up to a few dozens of photons. As shown by Reck [17], the number of beam splitters needed to implement an arbitrary $m \times m$ unitary matrix are $m(m-1)/2$. These have been implemented in bulk optics [18] and in integrated platforms [19–21]. Other non-universal approaches have been implemented in bulk optics [22] and in fibre architectures [23, 24], the largest to date being a bulk optics interferometer with 144 input/output modes [15]. Ideally, an interferometer should be lossless, reconfigurable and scalable in the number of input and output modes. A recent proposal [25] suggested using the temporal modes to encode the information as a means to scale up for Boson Sampling experiments. This scheme is attractive for its scalability and reconfigurability [18], whilst exhibiting comparable losses [26, 27] to the other reconfigurable platforms [21]. Furthermore, in this approach, the number of components is fixed regardless of the size of the implemented unitary. In principle, arbitrary scale can be achieved with minor additional hardware. Alternative non-universal time-bin interferometers have been proposed to achieve quantum supremacy via high-dimensional GBS [28].

In this work, we (i) implement a 20-mode time-bin interferometer to conduct a GBS experiment, and (ii) experimentally show how such GBS device can enhance the search for dense subgraphs. In particular, we demonstrate this for subgraphs of sizes three and four in a graph of ten nodes. This constitutes the first experimental realisation of GBS in a time-bin encoded manner and the first practical usage of a GBS machine to improve the search of dense subgraphs.

The paper is structured as follows. First, we introduce the main concepts, namely Gaussian Boson Sampling, the time-bin interferometer approach and the idea of using GBS to speed up the search for dense subgraphs in

a graph. Then, we move on to describe the experimental work, which combines these three elements and show the results obtained. To complement these, we perform numerical calculations to study the role of imperfections for the particular application of finding dense subgraphs.

II. THEORY

A. Gaussian Boson Sampling

Figure 1(a) illustrates the concept of Gaussian Boson Sampling. We consider an m-mode system with separable Gaussian state inputs that undergoes a transformation characterised by the transfer matrix Λ, followed by single-photon detection. The input states, $|\xi_i\rangle$, can be chosen from the spectrum of Gaussian states, namely, vacuum, squeezed vacuum, coherent or thermal states. The transfer matrix only consists of linear terms and loss, which are Gaussian transformations [29]. Therefore, the state at the output is also Gaussian and can be completely described by a $2m \times 2m$ covariance matrix, $\boldsymbol{\Sigma}$, and a displacement vector, $\boldsymbol{\alpha}$. In this context, the probability to measure a certain output pattern $\boldsymbol{n} = (n_1, n_2, n_3, \ldots, n_m)$ is given by [7]

$$P(\boldsymbol{n}) = \frac{P(0)}{\prod_i n_i!}\mathrm{Haf}(\boldsymbol{A}_{\boldsymbol{n}}), \tag{1}$$

where $P(0)$ is the probability of not detecting any photons at the output and Haf is the Hafnian function. The Hafnian of a matrix is computed as

$$\mathrm{Haf}(\boldsymbol{A}) = \sum_{M \in \mathrm{PMP}(n)} \prod_{(i,j)\in M} A_{i,j} \tag{2}$$

where PMP indicates the set of perfect matching permutations of n objects. The matrix $\boldsymbol{A}$ can be derived from the covariance matrix as

$$\boldsymbol{A} = \boldsymbol{X}(\boldsymbol{I} - \boldsymbol{Q}^{-1}), \tag{3}$$

where

$$\boldsymbol{X} = \begin{pmatrix} 0 & \boldsymbol{I} \\ \boldsymbol{I} & 0 \end{pmatrix} \quad \text{and} \tag{4a}$$

$$Q = \boldsymbol{\Sigma} + \boldsymbol{I}/2, \tag{4b}$$

where $\boldsymbol{I}$ is the identity matrix of appropriate dimension. The submatrix $\boldsymbol{A}_{\boldsymbol{n}}$ is obtained by selecting n_i times the i-th and $i+m$-ith rows and columns of $\boldsymbol{A}$. Subsequently, $\boldsymbol{A}_{\boldsymbol{n}}$ is a square matrix that grows with the total number of detected photons N, with $N = \sum_i n_i$. The matrix $\boldsymbol{A}$ can be decomposed into a block matrix of the form,

$$\boldsymbol{A} = \begin{pmatrix} \boldsymbol{B} & \boldsymbol{C} \\ \boldsymbol{C}^{\mathbf{T}} & \boldsymbol{B}^{*} \end{pmatrix}, \tag{5}$$

where $\boldsymbol{B}$ is a $m \times m$ symmetric matrix and $\boldsymbol{C}$ is a $m \times m$ Hermitian matrix.

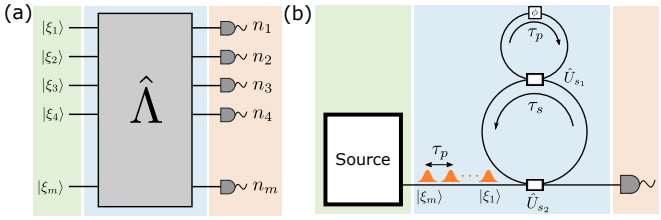

FIG. 1. (a) General GBS picture, where we have an m-mode Gaussian state going into an interferometer described by $\hat{\Lambda}$ and is then detected using single-photon detectors. (b) Time-bin encoded architecture to implement Gaussian Boson Sampling experiments. The modes are defined by temporal bins, and the interferometer is implemented by the double-loop structure. We just need one light source to generate the multimode input state, and we can detect the output state by using only one single-photon detector.

In the particular case of having a pure Gaussian state with no displacement at the output, $\boldsymbol{A}$ can be further reduced to $\boldsymbol{A} = \boldsymbol{B} \oplus \boldsymbol{B}^{*}$, i.e. $\boldsymbol{C} = 0$, and the probability to measure a detection pattern $\boldsymbol{n}$ becomes

$$P(\boldsymbol{n}) = \frac{P(0)}{\prod_i n_i!}|\mathrm{Haf}(\boldsymbol{B}_{\boldsymbol{n}})|^2, \tag{6}$$

where the submatrix $\boldsymbol{B}_{\boldsymbol{n}}$ is obtained by selecting n_i times the i-th rows and columns. Note that in this case, the matrix $\boldsymbol{B}_{\boldsymbol{n}}$ will be of size $N \times N$ and, due to the nature of the Hafnian, N needs to be even. This agrees well with the fact that if there is no loss present in the system, which would add mixedness to the state, photons will always come in pairs from the squeezed vacuum states and, therefore, detecting an odd number of photons will not be possible.

B. Time-bin interferometer

Here we introduce the time-bin interferometer [25], motivate its usage and explain how it can implement an arbitrary unitary. Fig. 1(b) exhibits an abstract representation of the end-to-end proposed architecture. We can distinguish three main parts, the light source, the interferometer and the detection scheme.

The fact that we only need a single source to run the whole experiment, as opposed to many sources [5, 19] or de-multiplexing techniques [20, 22], poses a significant simplification in terms of experimental resources. The laser system pumping the source will define the different temporal modes, meaning that to enlarge the size of the problem, we only need to let more pulses into the interferometer. For instance, a Ti:Sapphire laser with a repetition rate on the order of a few MHz and pulses of picoseconds could be employed.

The interferometer consists of two loops arranged in a "snowman"-like configuration, the lower one is the "storage" loop and the upper one is the "processing" loop.

The length of the processing loop is matched to the separation between consecutive pulses τ_p, while the storage loop must accommodate all the interfering m modes. We will consider its length to be an integer number of times τ_p. The two loops are connected via a variable beam splitter, s_1, and to the input/output mode through a fast switch, s_2. Note that s_2 has a dual purpose: coupling the input photons into the interferometer and setting the remaining modes to vacuum, i.e. acting as a shutter. The main distinction between s_1 and s_2 is the number of possible reflectivities each of them needs to be able to achieve. s_2 only acts as a switch, so it has an on/off behaviour, whereas s_1 is the beam splitter that will implement the unitaries and, therefore, needs to be able to cover a large range of possible splitting ratios. In fact, even if we are limited by the possible values s_1 can realise, this architecture is still universal, as proven by Aaronson and Bouland [30] and Sawicki [31]. However, this scenario is not appealing experimentally since the number of layers required to implement a certain unitary would be significant, implying more loss.

Finally, we have the detection system. This presents another substantial improvement of this architecture over other platforms. Due to the temporal encoding of the information, we can potentially reduce the required number of detectors to one, compared to the spatial encoding depicted in Fig. 1(a) in which we need m. This feature can become very relevant when scaling up to bigger interferometers. The main practical consideration is the reset time of the detectors being larger than the time-bin spacing, which could skew the output statistics.

Here we show how this approach can implement any multimode interferometer [25, 26]. The processing loop allows us to interfere consecutive modes, whilst the storage loop enables the procedure to be repeated as many times as required. The circuit in Fig. 2(a) describes the explicit interaction with the processing loop, mode $\mathcal{A}$, for one pass through the storage loop, where B_i corresponds to a general SU(2) operation – a phase shifter followed by a Mach-Zehnder interferometer, for instance. The SWAP operation couples the corresponding mode into the loop mode, $\mathcal{A}$. We assume that s_1 can implement any arbitrary SU(2) operation. Each of the numbered modes, except from $\mathcal{A}$, corresponds to a temporal mode. Conveniently, we can disregard the auxiliary mode employed for the interference, $\mathcal{A}$, and rewrite the system in terms of a Reck decomposition [17], as shown in Fig. 2(b). It is clear then, that by applying this operation $m-1$ times we can accomplish any arbitrary $m \times m$ unitary. Hence, this snowman structure is universal for linear optics. A similar configuration can be used to optimally implement the Clements decomposition [32, 33]. A relevant feature of the time-bin interferometer implementation is the non-uniformity of the loss incurred across the different temporal modes [27]. In general, this limits the ability to implement an arbitrary unitary [27]. In this case, balancing out the loss among all modes, at the expense of detection rates, is not possible.

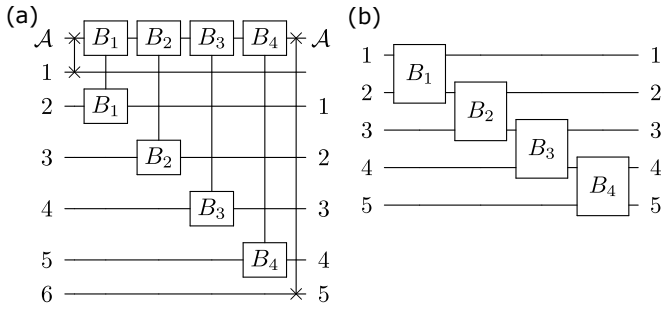

FIG. 2. (a) Explicit circuit of a pass through the processing loop. As per convention, the x symbol refers to the SWAP operation. (b) Simplified circuit of a single pass through the processing loop. The mode labels refer to time-bin modes, except for $\mathcal{A}$ that is the processing loop mode, and B_i represents beam splitter operation.

C. Finding dense subgraphs using a GBS device

A graph can be fully described by its adjacency matrix $\boldsymbol{\Delta}$, where the matrix elements Δ_{ij} determine the weight of the edge between nodes i and j, defining the connectivity between all nodes. For the case of an undirected graph, $\boldsymbol{\Delta}$ will be a symmetric matrix, i.e. $\Delta_{ij} = \Delta_{ji}$.

As we saw earlier in Eq. (5), the $\boldsymbol{A}$ matrix of a pure Gaussian state can be reduced to a matrix formed only by a symmetric matrix, $\boldsymbol{B}$, as $\boldsymbol{A} = \boldsymbol{B} \oplus \boldsymbol{B^*}$. In the case of no displacements, this matrix fully describes the Gaussian state. This naturally establishes a mapping between the adjacency matrix of a graph G, $\boldsymbol{\Delta}$, and the matrix describing a pure Gaussian state, $\boldsymbol{B}$. In this regard, if we can find a feature of a graph that is linked to the calculation of the Hafnian of its adjacency matrix, we will be able to use a GBS device to obtain some useful information about a graph. Indeed, Equation (2) provides a connection between the connectivity of an unweighted graph, described by the number of perfect matchings, and the Hafnian.

We can define the density of a weighted graph, G, as

$$D(G) = 2\frac{\sum_{i \in E_G} w_i}{|V_G|(|V_G|-1)}, \tag{7}$$

where w_i are the weights of the edges of G, E_G, and $|V_G|$ are the number of vertices in G. For an unweighted graph, i.e. $w_i \in 0, 1$, the density is bounded between 0 for an unconnected graph and 1 for a fully connected, or complete, graph with $w_i = 1\ \forall i$. It was recently shown by Arrazola and Bromley [13], that the number of perfect matchings is related to the density of a graph, and, therefore, so is the Hafnian of a fully positive (or negative) matrix. The higher the number of perfect matchings the denser the graph will be. This means that we can employ a GBS device to generate samples from a certain problem matrix, and that these will form dense subgraphs of the graph described by $\boldsymbol{B}$ with high probability. They show that this strategy can enhance the search over uniform

random searches or when using these samples as seeds in more elaborate algorithms, for instance, simulated annealing. More generally, this constitutes an example of the enhancement provided by using proportional sampling over random search in specific optimisation problems, as shown in [34].

The recipe for employing a GBS device for this purpose is given in [14] as follows:

1. Decompose $\boldsymbol{A}$ into a unitary matrix $\boldsymbol{U}$ and a vector $\boldsymbol{\lambda}$ using the Takagi-Autonne decomposition. These will correspond to the linear interferometer and squeezing parameters at each of the input modes, respectively.

2. Compile $\boldsymbol{U}$ into the appropriate beam splitter and phase-shifting operations of the linear interferometer. Program the interferometer accordingly.

3. Rescale the squeezing parameters $r_i = \tanh^{-1}(c\lambda_i)$ according to the constant $c > 0$ such that $\langle n \rangle = \sum_{i=1}^{m} \frac{(c\lambda_i)^2}{1-(c\lambda_i)^2}$. In the case of an n-node subgraph, this can be used to maximize the probability of obtaining an n-fold coincidence at the output. Note that this rescaling does not change the n-fold relative probability distribution.

4. Program the squeezers accordingly.

After following this procedure the GBS device will output samples, $\boldsymbol{n}$, with probability

$$P(\boldsymbol{n}) \propto c^N |\mathrm{Haf}(\boldsymbol{B_n})|^2 \tag{8}$$

where $N = \sum_i n_i$ and we assume that we are in the collision-free regime, i.e. $n_i = 0, 1\ \forall i$. We can then feed these samples into a classical algorithm to find dense subgraphs in a graph, for instance, as shown in [13].

An unavoidable imperfection in optical systems is loss. In experiments involving single-photon states, as is the case of standard Boson Sampling, uniform loss in the interferometer can be neglected by post-selecting on the same number of photons as we had at the input. So, in this scenario, loss will ultimately affect our detection rates solely, but the probability distribution at the output for some n-fold detection will remain unaffected. The situation is rather different when employing other types of input states, for instance, single-mode squeezed vacuum (SMSV). In the case of GBS, it is easy to see that if we have loss in the system, we will not have a pure state anymore, and, therefore, $\boldsymbol{C} \neq 0$ and we would be sampling from a different distribution. The impact on how this imperfection affects our ability to use GBS to find dense subgraphs in a graph is studied later in Sec. V.

III. EXPERIMENT

Fig. 3 shows a schematic of the setup employed in the experiment. A Ti:Sapphire mode-locked laser produces

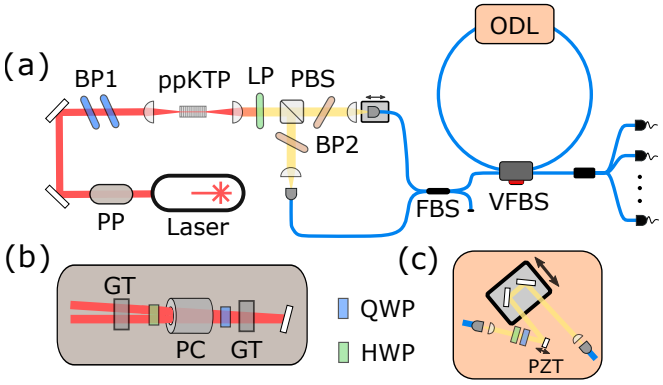

FIG. 3. (a) Main experiment setup. PP: pulse-picker, BP1: bandpass filters at 775 nm, PBS: polarising beam-splitter (Wollaston prism), BP2: bandpass filters at 1550 nm, FBS: fibre beam splitter, VFBS: variable FBS and ODL: optical delay line. (b) Detailed schematic of the pulse-picking system, indicated as PP in (a). GT: Glan-Taylor polariser, PC: Pockels cell, QWP: quarter-wave plate and HWP: half-wave plate. (c) Detailed schematic of the free-space optical delay in the single-loop interferometer, indicated as ODL in (a). PZT: piezoelectric actuator.

100 fs pulses at a repetition rate of 80 MHz. A Pockels cell-based pulse picker is used to define the temporal modes of interest and reject groups of pulses in order to initialise the loop to vacuum. A pair of angle-tuned bandpass filters shape the spectrum of the incoming pump pulses appropriately to obtain degenerate and factorable emission via spontaneous parametric down-conversion (SPDC) from a type-II periodically poled potassium titanyl phosphate (ppKTP) waveguide [35–37]. The two fields of the two-mode squeezed vacuum (TMSV) state generated in the nonlinear process are split using a Wollaston prism and coupled into polarisation-maintaining (PM) single-mode fibre. Rotating the polarisation of one of the fields and using a fibre-based PM 50:50 beam splitter, we recombine the two fields to generate SMSV states. In this case, the two output fields do not exhibit any correlation and we can block one of them and use the other for the time-bin interferometer, preserving its purity. We send one of the outputs to the single-loop interferometer, which consists of an evanescent-field variable fibre coupler and a fibre-based loop. The length of the loop is matched to the repetition rate of the laser by using a free-space optical delay with a motorised stage, as shown in Fig. 3(c). The phase of the loop is controlled using a mirror mounted on a piezoelectric actuator. Finally, the output state from the loop interferometer is analysed using pseudo-photon-number resolving techniques via a spatially-multiplexed detector.

The pulse-picking system, shown in Fig. 3(b), sets the clock-time of the experiment and uses a repetition rate of 200 kHz. The pulse configuration of the Pockels cell lets ten pulses of vacuum, ten occupied pulses and then ten more pulses of vacuum. We are interested in those last 20 time-bins, comprising a total time of 250 ns. This means

that we are restricting ourselves to an effective duty cycle of 5% of the available pulses. We gate the timetagger system to only record time tags in this region, reducing the required analysis time substantially. See Appendix B for further details on this setup.

The two fields from the SPDC are coupled into single-mode fibres with an efficiency of $\eta_c = 40\%$, without including detection efficiencies. The main limitation here is the mode mismatch between the fibre and the waveguide modes, estimated to be between 60-70%. We can identify two main sources of loss in the interferometer, the VFBS, with a throughput of $\eta_f = 90\%$ and the loss in the free-space ODL, with an efficiency of $\eta_o = 80\%$. Finally, the detection efficiency of the SNSPDs is maximised by using fibre polarisation controllers to be on average $\eta_d = 80\%$.

The purity of the output state, see Appendix A, is 98%. Therefore, it can be well approximated by a TMSV state, which can be expressed in the Fock basis as

$$|\text{TMSV}\rangle = \sqrt{1-\lambda^2}\sum_{n=0}\lambda^n|n,n\rangle, \tag{9}$$

where $\lambda = e^{i\theta}\tanh(r)$ and r and θ are the squeezing and phase parameters, respectively. In the ideal case, interfering the idler and signal modes in a beam splitter gives an SMSV state in each output arm, namely

$$|\text{SMSV}\rangle = \frac{1}{\sqrt{\cosh(r)}}\sum_{n=0}^{\infty}\frac{\sqrt{(2n)!}}{2^n n!}\left[-e^{i\theta}\tanh(r)\right]^n|2n\rangle \tag{10}$$

where the squeezing in each arm is the same as that of the TMSV. The quality of the SMSV will be limited by the interference visibility between the two modes from the TMSV source. To assess this, we perform a Hong-Ou-Mandel measurement between the two fields. From a measurement of the marginal spectrum for each field, see Appendix A, we observe a slight mismatch in central wavelengths and bandwidth, leading to some distinguishability. The discrepancy in the bandwidth between the two fields originates from the group velocities in pp-KTP not being symmetric with respect to that of the pump [35]. The Hong-Ou-Mandel measurement reveals a visibility of 95.3(2)%, indicating good indistinguishability. We use different squeezing values for the SMSV state, namely $\lambda = \{0.22, 0.31, 0.43\}$.

The main motivation behind the use of a single-loop structure, despite its simplicity, is the ability to apply a transformation involving a large number of modes. Fig. 4(a) shows an estimation of the transfer matrix applied by the single-loop interferometer for $\phi = 0$, where ϕ is the phase of the loop. Due to the nature of the single-loop, this is an upper-diagonal matrix since it is not possible to inject a photon at time-bin i and detect it at output j for $i > j$. By varying the reflectivity of the VFBS, we can change the transformation matrix to some extent. In this case, this was arbitrarily set to $T = 50\%$. Likewise, Fig. 4(b), shows the modelled $\boldsymbol{A}$ matrix where, as shown, the $\boldsymbol{C}$ matrix is non-zero, denoting the mixedness

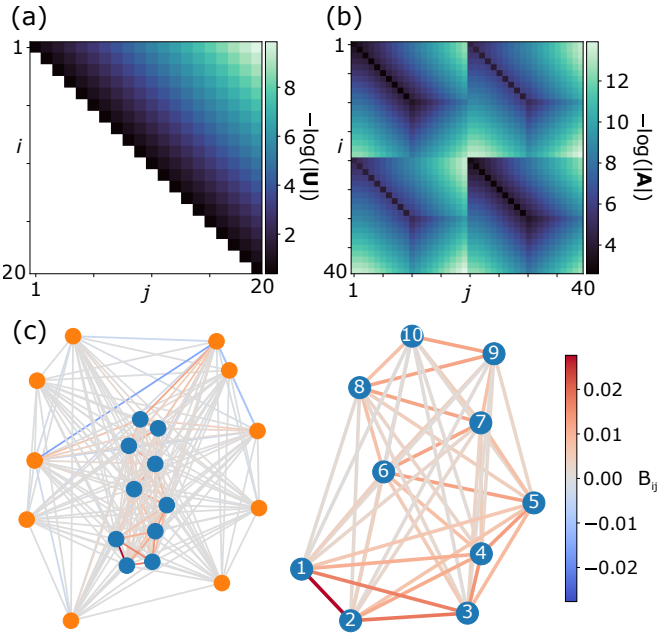

FIG. 4. (a) Transformation matrix corresponding to the single loop transformation. (b) A matrix of the output state after the single-loop transformation. We can clearly see that the state corresponds to a non-pure Gaussian state, i.e. $\boldsymbol{C} \neq 0$. (c) (Left) Graph, G_T, defined by taking the symmetric part, $\boldsymbol{B}$, of the $\boldsymbol{A}$ matrix modelled from the experiment as the adjacency matrix. The blue dots indicate the fully positive subgraph shown on the right. (Right) Fully positive subgraph, G_P, of G_T given by nodes 1-10. The colorbar indicates the weights of the edges.

of the Gaussian state. The piezoelectric actuator allows us to change ϕ and perform active phase-locking, see Appendix C for details. Setting $\phi = 0$ makes both $\boldsymbol{U}$ and $\boldsymbol{A}$ to be real-valued matrices.

We employ a spatially-multiplexed array of eight superconducting nanowire single-photon detectors to be able to perform pseudo-photon number resolving detection. Due to the reset time of the detectors, 60 ns, being greater than the spacing between time-bins, 12.5 ns, this type of spatially-multiplexed detection is necessary to be able to resolve detections in consecutive time-bins. This will impact the output detection probability. As an example, take the output state $[1, 2]$ (one detection in the first time-bin, and another in the second time-in). This event will be less likely than $[1, 10]$ (second detection in the tenth time-bin) since there is a greater chance of the detector being unresponsive due to the detector dead-time. Employing a higher number of detectors in this configuration would diminish this effect.

IV. RESULTS

We begin by studying the output photon statistics of our device and quantifying the discrepancy between the

experimental data and the theoretical model. Then, we use the samples produced by the experimental device to demonstrate an enhancement in the search of dense subgraphs when using these over using uniform random samples.

A. GBS output statistics

We model our experiment using the StrawberryFields python package [38]. For this, we use the parameters of the loss mentioned above, which are measured independently or given by the manufacturer. To assess the validity of the model, we compute the total variation distance (TVD), defined as

$$D(p,q) = \frac{1}{2}\sum_i |p_i - q_i|, \tag{11}$$

where p and q are the two probability distributions we are comparing. The TVD gives a measure of how close the probability distributions are. It ranges from 0 to 1 for identical to completely non-overlapping distributions, respectively. We minimise the TVD for the twofold detections to infer the value of the squeezing at the input. After this, for the $\lambda = 0.31$ case, we obtain a TVD between the model and the experiment, $D(P_{\text{th}}, P_{\text{exp}})$, of 0.0758(3) and 0.081(1), for the twofold and threefold coincidences, respectively, indicating the model does a good job in describing the experiment. To calculate the probabilities from the model, we use Eq. (1). Fig. 5 shows a plot with the (a) twofold and (b) threefold probabilities obtained from the experiment and given by the model. As can be observed, the very well defined pattern of $\boldsymbol{U}$, with an exponential decay, is displayed in these distributions. In both cases, we see good agreement between the theory and the experiment. The detection rates of threefold and fourfold detections are 300 Hz and 10 Hz, respectively. Note that the experiment rate is 200 kHz with a duty cycle of 5%, limited by the Pockels cell. By overcoming these limitations, these rates could be increased by a factor of 20 for the same level of squeezing.

B. Finding dense subgraphs

Here we experimentally demonstrate that a GBS device can be used to enhance the search for dense subgraphs in a graph. For the purpose of identifying dense subgraphs using GBS, we require the adjacency matrix of the graph to be fully positive or negative, such that the Haf is proportional to the density as given in Eq. (7). For this, we focus on a subgraph of the graph defined by the symmetric part of matrix $\boldsymbol{A}$, i.e. the $\boldsymbol{B}$ matrix. We choose the subgraph containing nodes 1-10, which corresponds to time-bins 1-10. Fig. 4(c) shows both the complete graph (left) and the fully positive subgraph defined by nodes 1-10 (right) corresponding to the $\boldsymbol{B}$ matrix of

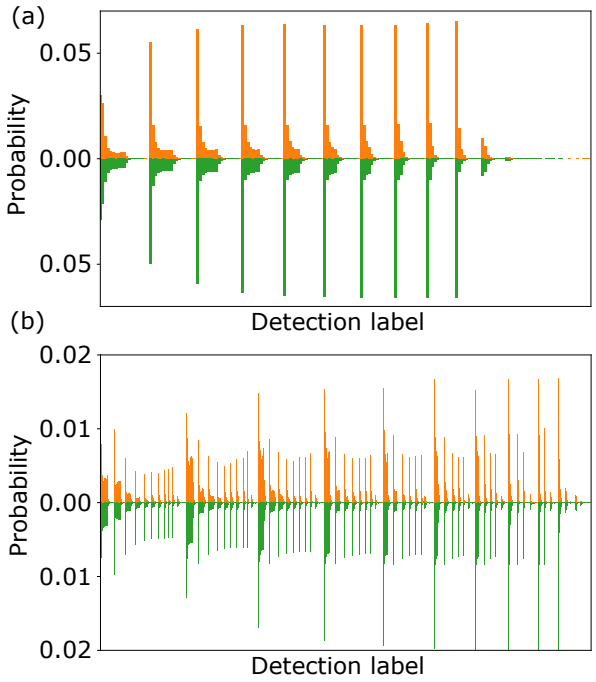

FIG. 5. Probability distribution for the twofold (a) and threefold (b) detections with an input squeezing of $\lambda = 0.31$. Green bars show the theory values and orange bars the experimental data. The x-axis detection labels are sorted in ascending order from left to right, i.e. $\{[1,1], [1,2], \ldots, [19,20], [20,20]\}$ and $\{[1,1,1], [1,1,2], \ldots, [19,20,20], [20,20,20]\}$, respectively.

the $\lambda = 0.31$ case of the experiment. The complete graph corresponds to the top left corner of $\boldsymbol{A}$ with the weights of the edges indicated by the colouring. Since we are interested in nondegenerate k-node subgraphs, we filter the obtained samples to only select nondegenerate k-fold detections. In this particular case, due to the nature of the interferometer, this has a substantial impact on the detection rates. After this postselection, we are left with 107, 312 and 1802 nondegenerate fourfold samples for $\lambda = \{0.22, 0.31, 0.43\}$ with integration times of 8h, 3h and 3h, respectively.

Similar to [13], we take the postselected GBS samples and use them as seeds in a classical algorithm to search for dense subgraphs, in this case, a random search. In the random search algorithm, we draw n samples, each containing k nodes, from the appropriate distribution, calculate the density corresponding to each sample, and select the one with the maximum density. We vary the number of samples n drawn and, for each of these values, repeat the procedure 400 times to remove statistical fluctuations. Fig. 6 shows the mean density obtained as a function of the number of samples drawn for subgraphs of size three (a) and size four (b). We see that in both cases the GBS-enhanced protocols perform better than the uniform sampling case, this improvement being more prominent in the 4-node subgraph case. To compare the performance of the algorithm for the dif-

ferent input seeds, we consider the number of samples needed, on average, to find a graph whose density is 95% of the maximum and the mean density achieved for a given number of samples. The results are summarised in Table I and give a quantitative value of the speedup provided by the GBS device.

Moreover, as observed, imperfections in the experiment, mostly due to optical loss, degrade the performance of the algorithm, as indicated by the ideal curve in (b), which would correspond to the lossless scenario. In this case, the samples are drawn directly from the distribution given by $|\mathrm{Haf}(\boldsymbol{B_n})|^2$. For the threefold case, where the Hafnian would be null due to the number of detections being odd, we use the fourfold distribution and remove one detection at random. Interestingly, we also notice that when increasing the squeezing the speed at which the curve approaches the maximum mean density decreases. Table I quantitatively illustrates this observation. This effect is studied in more detail in Section V.

TABLE I. Comparison between the performance for the different sources of samples (seeds) in the random search algorithm. We consider two metrics: the number of samples needed to achieve a mean density of 95% and the density achieved when using 50 samples.

n	Seed	Samples at 95% den.	Density for 50 samp.
3	Ideal	34(1)	0.020(0)
3	$\lambda = 0.22$	92(3)	0.0186(1)
3	$\lambda = 0.31$	99(3)	0.0182(1)
3	$\lambda = 0.43$	117(4)	0.0180(2)
3	Stochastic	178(5)	0.0167(2)
4	Ideal	14(1)	0.0164(0)
4	$\lambda = 0.22$	62(3)	0.0153(0)
4	$\lambda = 0.31$	98(3)	0.0143(1)
4	$\lambda = 0.43$	143(5)	0.0140(1)
4	Stochastic	> 260	0.0130(1)

V. LOSS AND SQUEEZING TRADE-OFF

In this section, we study how imperfections affect GBS outputs and, in particular, impact the performance of the classical algorithm to find dense subgraphs. In essence, these imperfections will change the probability distribution we are drawing our samples from, but how this modifies the performance of the algorithm for this task is not clear. Previous work [39] has focused on methods to mitigate the effect of loss in the probability distribution, although for large systems performing the additional measurements required for this strategy may prove challenging. Here, we focus on the most prominent imperfection in conventional GBS experiments: uniform loss at the input. We acknowledge that other errors such as deviations from the expected unitary or mode-dependent losses are also possible, but we leave these for future work.

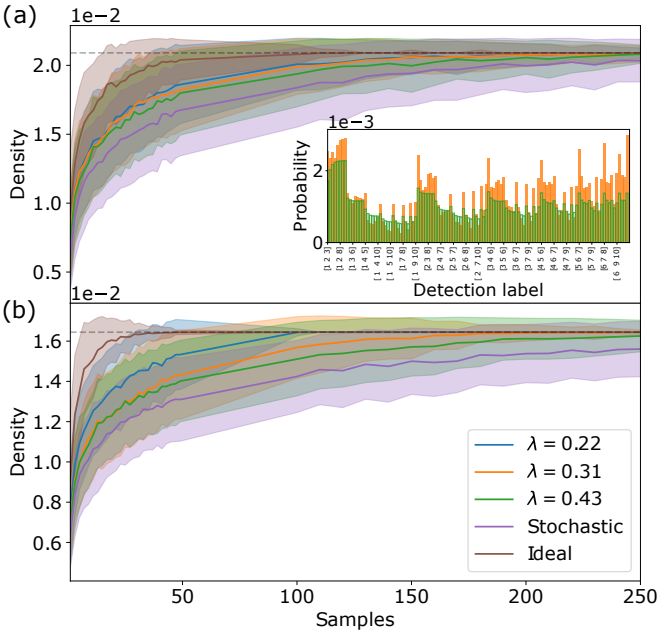

FIG. 6. (a) Density of the 3-node subgraph as a function of the number of samples chosen. The inset shows the probability distribution for the nondegenerate output states of the experimental samples (orange filling) and the theoretical model (green edge). (b) Density of the 4-node subgraph as a function of the number of samples. The purple line indicates a uniform random search, the blue, orange and green lines use samples obtained from the GBS experiment for different values of the squeezing as indicated in the legend, and the brown line indicates samples obtained when sampling from the distribution obtained from $|\mathrm{Haf}(\boldsymbol{B_n})|^2$. The dashed line indicates the density of the densest subgraph. The search speed decreases when increasing the squeezing. This effect is further studied in Sec. V.

To study the role of imperfections we use the general following procedure

1. Construct the graph for which dense subgraphs are to be found. It is generated by creating two Erdos-Renyi graphs, a small one with high edge probability and a larger one with low edge probability. Then we connect the nodes of the smaller graph to the nodes of the larger one at random [13].

2. We perform a Takagi-Autonne decomposition to obtain the squeezing parameters and unitary matrices that encode this graph onto the GBS device. We appropriately rescale the squeezing values to change the mean photon number per mode at the output.

3. Modify the circuit appropriately, e.g. adding optical loss at the modes, to effectively study how the imperfections affect the output probabilities. We investigate how this probability distribution deviates from the lossless case.

4. Generate samples according to those probabilities

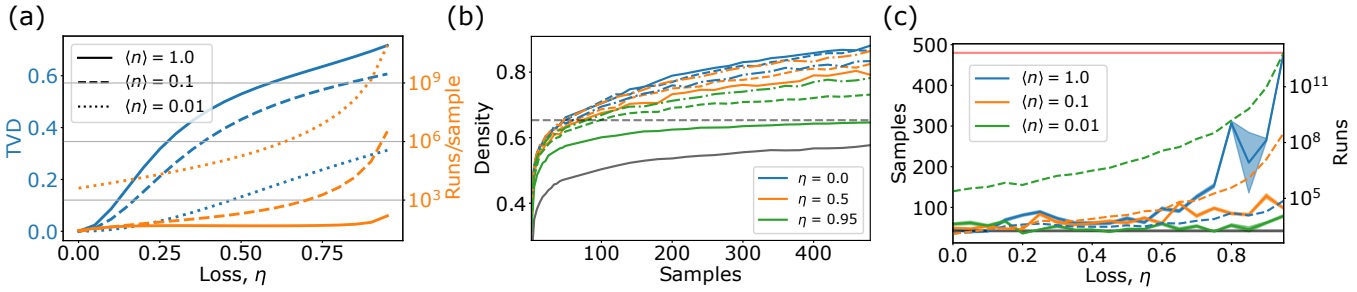

FIG. 7. (a) TVD and runs/samples as a function of the input loss for several mean photon numbers per mode at the output. (b) Density as a function of the number of samples used in the random search algorithm for several mean photon numbers indicated in the legend of (a). The different colours correspond to different input losses in the system while the black curve shows the performance of the algorithm when using uniform random samples. (c) Number of samples (solid) and runs (dashed) needed to achieve a certain mean density, defined by the black dashed line in (b), as a function of the input loss for several mean photon numbers. The shaded areas correspond to one standard deviation of the mean. The black line indicates the density achieved by the algorithm when using samples drawn directly from the adjacency matrix of the graph and the red line corresponds to uniform drawn samples. The shaded areas correspond to one standard deviation of the mean.

and feed them into the random search algorithm previously described to find dense subgraphs. Repeat this for a different number of input samples.

5. Find the number of samples needed to achieve a mean density over the n repetitions to be above a certain threshold and the density achieved with some number of samples.

Here, we focus on a graph consisting of 26 nodes, where six of these have been implanted in the graph. The parameters used to generate these Erdos-Renyi graphs are: $N_A = 20$, $N_B = 6$, $p_A = 0.3$ and $p_B = 0.875$, where p_i is the probability of two vertices in graph $i \in \{A, B\}$ to be connected by an edge. For the random search algorithm, we repeat the search for 1000 iterations to minimise statistical fluctuations on the mean as much as possible.

First, we focus on how these imperfections modify the normalised probability distribution for a given n-fold detection. To evaluate this, we use the TVD, shown in Eq. (11). In other types of experiments, where we have a well-defined number of input photons, e.g. Boson Sampling, these probability distributions remain independent of loss. Fig. 7(a) shows the TVD and the average number of runs needed to obtain a 6-fold sample, i.e. $1/p(6)$ where $p(6)$ is the probability to obtain a collision-free 6-fold detection at the output, as a function of the loss for several mean photon numbers per mode, i.e. $\langle n \rangle = 1/m \sum_i \langle n_i \rangle$ where m is the number of modes. We observe that as the loss increases, the deviation from the lossless case is more pronounced for those cases in which the squeezing was high, whereas much smaller for those cases where the squeezing was low. When the squeezing is low, we can truncate the superposition of even number Fock states at $|n\rangle \to 2$, in the low squeezing limit, and, hence, the impact of higher-order photon numbers being affected by loss is negligible.

Considering the number of runs per 6-fold sample, runs/sample from hereon, we see that the degradation in the TVD presents a clear trade-off between state fidelity to the lossless case and detection rates. We proceed to study how this trade-off manifests in the search for dense subgraphs and if, at some point, allowing more runs/samples can lead to a substantial decrease in the TVD that is beneficial to this problem. As mentioned, an alternative to reducing the squeezing may be error mitigation [39]. This procedure involves either changing the experimental loss parameter to interpolate the measurements or performing classical postprocessing of the data.

Similar to Fig. 6, Fig. 7(b) shows the density obtained with n samples using a random search algorithm for several values of input loss (different line colours) and different mean photon numbers (different line styles). The grey dashed line indicates the value for the density we use to calculate the data shown in Fig. 7(c). As observed, for a constant value of the loss, the performance of the algorithm diminishes with increasing values of squeezing, in good agreement with the experimental observations. Fig. 7(c) shows the point where the mean density achieved by each of the curves in (b) crosses the dashed line, i.e. achieves a mean value of 75 %, as a function of loss for different mean photon numbers. The speed at which the algorithm reaches a certain value for the mean density degrades as a function of the input loss for high squeezing values, but it remains unaffected when the squeezing is small. Note that in all cases, the GBS device still outperforms the uniform sampling approach indicated by the solid grey line. The dashed lines indicate the number of experimental runs needed to achieve the required number of samples needed to obtain a mean density. As shown, because the number of runs/sample increases exponentially with the mean photon number $\langle n \rangle$, in the regime we have studied, increasing the squeezing reduces the number of runs needed, in general. Due to the statistical noise of the algorithm, it is hard to extract conclusions for regimes where the variations between av-

erage photon numbers are small. These results indicate that for large-scale dense subgraph searches, where high squeezing values are required, careful consideration of the impact of loss is needed. In some instances, it might even be advantageous to reduce the squeezing to get closer to the lossless case distribution, despite the sacrifice in detection rates.

VI. CONCLUSIONS

To summarise, we used a time-bin architecture to experimentally demonstrate that samples from a GBS device can be used to enhance the search for dense subgraphs over uniform random sampling techniques. We employed a time-bin interferometer and a source of SMSV to detect samples with up to four photons. The use of a time-bin configuration as opposed to a spatial mode interferometer allowed us to scale up the number of modes in a straightforward manner. From the generated symmetric $\boldsymbol{B}$ matrix, we identified a fully positive submatrix and mapped it into a graph through its adjacency matrix. By post selecting samples contained in the rows and columns of such submatrix, we showed that when feeding the random search algorithm with those samples, the speed at which we can find dense subgraphs is enhanced over uniform random samples.

We repeat this procedure for three different squeezing parameters, observing a degradation of the algorithm's performance with increasing squeezing. To understand this, we numerically studied the role of input loss in a GBS experiment and found that the TVD with respect to the lossless case increases when using a higher squeezing. We then investigated the impact of this in the search for dense subgraphs problem and showed that there exists a trade-off between squeezing and algorithm speed for high values of input loss. This is in good agreement with the experimental observations.

This work constitutes the first experimental demonstration of the implementation of GBS in a time-bin encoded architecture and of how a GBS device can be employed to speed up the search of dense subgraphs. We hope this work can motivate other research groups to scale up this application to the regime where using a GBS device gives a quantum advantage. In this sense, in-depth consideration of what the consequences of imperfections are in near-term applications using GBS devices is needed.

Time-bin encoded GBS, in a fibre-based interferometer, offers many practical advantages for achieving quantum speedups in certain application areas. Our work should encourage further theoretical studies of computational problems which map onto this architecture. It will stimulate the engineering of integrated fibre-based squeezed light sources [40] as well as low-loss switching, which is essential for performing arbitrary operations on time-bin encoded states.

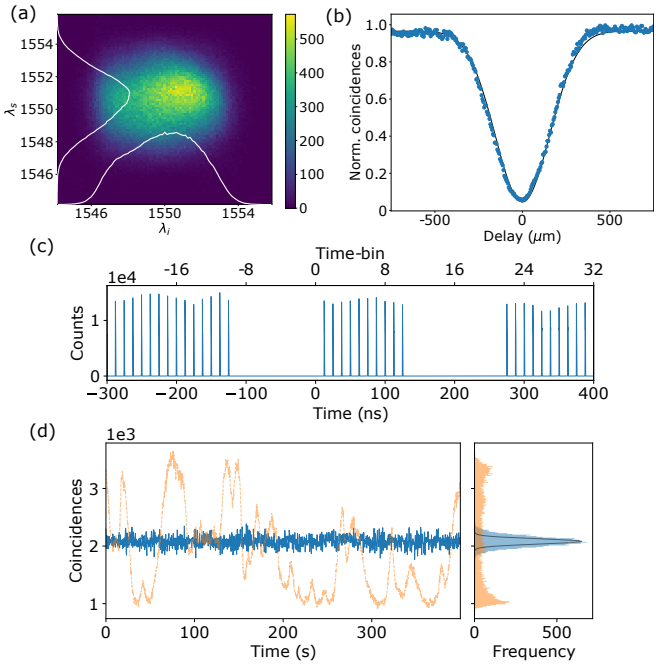

FIG. 8. (a) Joint spectral amplitude of the source. The colorbar indicates the number of counts. (b) Hong-Ou-Mandel interference between the idler and the signal. The error bars are derived from the Poissonian statistical error. The visibility is 95.3(2)%. (c) Histogram of the counts at the unused output port of the FBS, demonstrating the effectiveness of the pulse-picking system. (d) Twofold coincidences comparing the cases where we let the phase inside the loop fluctuate naturally (orange) and when we perform phase-locking (blue). The black line in the histogram indicates the fluctuations due to Poissonian statistics.

ACKNOWLEDGMENTS

This work was supported by: Engineering and Physical Sciences Research Council via the Quantum Systems Engineering Skills Hub and the Quantum Computing and Simulation Hub (P510257, T001062)

Appendix A: Source characterization

Here, we provide additional details about the source used to generate SMSV states. Fig. 8(a) shows the joint spectral intensity (JSI). The emission is degenerate and factorable, showing a purity of $\mathcal{P} = 98\%$. This measurement was performed using a time-of-flight spectrometer implemented using dispersion-compensating fibers followed by single-photon detectors. Fig. 8(b) shows the Hong-Ou-Mandel interference between the idler and signal fields from the source. This is implemented by measuring coincidences at the output of the beam splitter (FBS) in Fig. 3 when working in the low-squeezing regime. We obtain a visibility of 95.3(2)%, defined as $(C_{\max} - C_{\min})/C_{\max}$.

Appendix B: Pulse picker system

Fig. 3(b) shows a detailed schematic of the pulse-picking system. The beam passes through a Glan-Taylor (GT) polariser whose polarization axis is aligned with the light coming from the laser, then a half-wave plate (HWP) is used to set the polarization of the beam at 45° with respect to the optic-axis of the crystal of the Pockels cell. The Pockels cell consists of an X-cut 20 mm rubydium-tantalate phospate (RTP) crystal with an aperture of 3 mm and $V_\pi \sim 1$kV. The high-voltage driver of the Pockels cell is driven by a pulse generator at a repetition rate of 200 kHz. A quarter-wave plate (QWP) compensates for the natural birefrigence of the RTP crystal followed by another GT. The system is arranged in a double-pass configuration, to further increase the extinction ratio. Using it in this configuration we observe an extinction ratio of $1 : 10^5$. The overall transmission through the system is 70%. Fig. 8(c) shows a histogram of the counts after the pulse picker.

Appendix C: Phase-locking

Here we provide more details on the phase-locking. The probability of obtaining a coincidence at the output of the single-loop depends on the phase of the loop ϕ. We employ a piezoeletric stack (PK25FA2P2) with a maximum displacement, with no load, of 12 μm. We glue a 1/2" mirror to it and use a 0-75V amplifier driven by a NI DAQ card to control the voltage. We find that best results, in terms of optical alignment, without compromising the phase stability are achieved when driving the piezo in the range of 0-7 V. To perform the phase-locking, we use a PID controller where the error signal is obtained from a pregenerated calibration signal. We integrate the counts for 150 ms and update the voltage according to the PID outcome. Fig. 4(d) shows a comparison between the phase when we let it evolve naturally as opposed to when we actively control it. The standard deviation of the fluctuations when performing phase-locking is $2\sigma_P$, where σ_P is the standard deviation due to counting statistics.

[1] M. A. Nielsen and I. L. Chuang, *Cambridge University Press* (2010).

[2] T. D. Ladd, F. Jelezko, R. Laflamme, Y. Nakamura, C. Monroe, and J. L. O'Brien, Quantum computers (2010).

[3] P. W. Shor, SIAM Journal on Computing **26**, 1484 (1997), arXiv:9508027 [quant-ph].

[4] F. Arute, K. Arya, R. Babbush, D. Bacon, J. C. Bardin, R. Barends, R. Biswas, S. Boixo, F. G. Brandao, D. A. Buell, B. Burkett, Y. Chen, Z. Chen, B. Chiaro, R. Collins, W. Courtney, A. Dunsworth, E. Farhi, B. Foxen, A. Fowler, C. Gidney, M. Giustina, R. Graff, K. Guerin, S. Habegger, M. P. Harrigan, M. J. Hartmann, A. Ho, M. Hoffmann, T. Huang, T. S. Humble, S. V. Isakov, E. Jeffrey, Z. Jiang, D. Kafri, K. Kechedzhi, J. Kelly, P. V. Klimov, S. Knysh, A. Korotkov, F. Kostritsa, D. Landhuis, M. Lindmark, E. Lucero, D. Lyakh, S. Mandrà, J. R. McClean, M. McEwen, A. Megrant, X. Mi, K. Michielsen, M. Mohseni, J. Mutus, O. Naaman, M. Neeley, C. Neill, M. Y. Niu, E. Ostby, A. Petukhov, J. C. Platt, C. Quintana, E. G. Rieffel, P. Roushan, N. C. Rubin, D. Sank, K. J. Satzinger, V. Smelyanskiy, K. J. Sung, M. D. Trevithick, A. Vainsencher, B. Villalonga, T. White, Z. J. Yao, P. Yeh, A. Zalcman, H. Neven, and J. M. Martinis, Nature **574**, 505 (2019).

[5] H.-S. Zhong, H. Wang, Y.-H. Deng, M.-C. Chen, L.-C. Peng, Y.-H. Luo, J. Qin, D. Wu, X. Ding, Y. Hu, P. Hu, X.-Y. Yang, W.-J. Zhang, H. Li, Y. Li, X. Jiang, L. Gan, G. Yang, L. You, Z. Wang, L. Li, N.-L. Liu, C.-Y. Lu, and J.-W. Pan, *Science*, Tech. Rep. 6523 (2020) arXiv:2012.01625.

[6] V. Saggio, B. E. Asenbeck, A. Hamann, T. Strömberg, P. Schiansky, V. Dunjko, N. Friis, N. C. Harris, M. Hochberg, D. Englund, S. Wölk, H. J. Briegel, and P. Walther, Nature **591**, 229 (2021), arXiv:2103.06294.

[7] C. S. Hamilton, R. Kruse, L. Sansoni, S. Barkhofen, C. Silberhorn, and I. Jex, Physical Review Letters **119**, 170501 (2017), arXiv:1612.01199.

[8] R. Kruse, C. S. Hamilton, L. Sansoni, S. Barkhofen, C. Silberhorn, and I. Jex, Physical Review A **100**, 10.1103/physreva.100.032326 (2019), arXiv:1801.07488.

[9] S. Aaronson and A. Arkhipov, in *Proceedings of the Annual ACM Symposium on Theory of Computing*, 0844626 (2011) pp. 333–342, arXiv:1011.3245.

[10] I. Tzitrin, J. E. Bourassa, N. C. Menicucci, and K. K. Sabapathy, Physical Review A **101**, 32315 (2020), arXiv:1910.03673.

[11] J. Eli Bourassa, R. N. Alexander, M. Vasmer, A. Patil, I. Tzitrin, T. Matsuura, D. Su, B. Q. Baragiola, S. Guha, G. Dauphinais, K. K. Sabapathy, N. C. Menicucci, and I. Dhand, *Quantum*, Tech. Rep. (2021) arXiv:2010.02905.

[12] J. Huh, G. G. Guerreschi, B. Peropadre, J. R. Mcclean, and A. Aspuru-Guzik, Nature Photonics **9**, 615 (2015), arXiv:1412.8427.

[13] J. M. Arrazola and T. R. Bromley, Phys. Rev. Lett. **121**, 30503 (2018).

[14] T. R. Bromley, J. M. Arrazola, S. Jahangiri, J. Izaac, N. Quesada, A. D. Gran, M. Schuld, J. Swinarton, Z. Zabaneh, and N. Killoran, Quantum Science and Technology **5**, 34010 (2019), arXiv:1912.07634.

[15] H. S. Zhong, Y. H. Deng, J. Qin, H. Wang, M. C. Chen, L. C. Peng, Y. H. Luo, D. Wu, S. Q. Gong, H. Su, Y. Hu, P. Hu, X. Y. Yang, W. J. Zhang, H. Li, Y. Li, X. Jiang, L. Gan, G. Yang, L. You, Z. Wang, L. Li, N. L. Liu, J. J. Renema, C. Y. Lu, and J. W. Pan, Physical Review Letters **127**, 10.1103/PhysRevLett.127.180502 (2021), arXiv:2106.15534.

[16] J. M. Arrazola, V. Bergholm, K. Brádler, T. R. Bromley, M. J. Collins, I. Dhand, A. Fumagalli, T. Gerrits, A. Goussev, L. G. Helt, J. Hundal, T. Isacsson, R. B. Israel, J. Izaac, S. Jahangiri, R. Janik, N. Killoran, S. P.

Kumar, J. Lavoie, A. E. Lita, D. H. Mahler, M. Menotti, B. Morrison, S. W. Nam, L. Neuhaus, H. Y. Qi, N. Quesada, A. Repingon, K. K. Sabapathy, M. Schuld, D. Su, J. Swinarton, A. Száva, K. Tan, P. Tan, V. D. Vaidya, Z. Vernon, Z. Zabaneh, and Y. Zhang, Nature **591**, 54 (2021), arXiv:2103.02109.

[17] M. Reck, A. Zeilinger, H. J. Bernstein, and P. Bertani, Experimental Realization of Any Discrete Unitary Operator (1994).

[18] Y. He, X. Ding, Z. E. Su, H. L. Huang, J. Qin, C. Wang, S. Unsleber, C. Chen, H. Wang, Y. M. He, X. L. Wang, W. J. Zhang, S. J. Chen, C. Schneider, M. Kamp, L. X. You, Z. Wang, S. Höfling, C. Y. Lu, and J. W. Pan, Physical Review Letters **118**, 10.1103/PhysRevLett.118.190501 (2017), arXiv:1603.04127.

[19] J. B. Spring, B. J. Metcalf, P. C. Humphreys, W. S. Kolthammer, X.-M. M. Jin, M. Barbieri, A. Datta, N. Thomas-Peter, N. K. Langford, D. Kundys, J. C. Gates, B. J. Smith, P. G. R. R. Smith, and I. A. Walmsley, Science **339**, 798 (2013), arXiv:1212.2622.

[20] C. Antón, J. C. Loredo, G. Coppola, H. Ollivier, N. Viggianiello, A. Harouri, N. Somaschi, A. Crespi, I. Sagnes, A. Lemaître, L. Lanco, R. Osellame, F. Sciarrino, and P. Senellart, Optica **6**, 1471 (2019), arXiv:1905.00936.

[21] C. Taballione, R. van der Meer, H. J. Snijders, P. Hooijschuur, J. P. Epping, M. de Goede, B. Kassenberg, P. Venderbosch, C. Toebes, H. van den Vlekkert, P. W. H. Pinkse, and J. J. Renema, Materials for Quantum Technology **1**, 035002 (2021), arXiv:2012.05673.

[22] H. Wang, J. Qin, X. Ding, M.-C. Chen, S. Chen, X. You, Y.-M. He, X. Jiang, Z. Wang, L. You, C. Schneider, J. J. Renema, S. Höfling, C.-Y. Lu, J.-W. Pan, Z. Wang, C. Schneider, J. J. Renema, S. Höfling, C.-Y. Lu, and J.-W. Pan, Physical Review Letters **123**, 10.1103/PhysRevLett.123.250503 (2019).

[23] J. Boutari, A. Feizpour, S. Barz, C. D. Franco, M. S. Kim, W. S. Kolthammer, and I. A. Walmsley, Journal of Optics (United Kingdom) **18**, 10.1088/2040-8978/18/9/094007 (2016), arXiv:1607.00891.

[24] M. A. Broome, A. Fedrizzi, S. Rahimi-Keshari, J. Dove, S. Aaronson, T. C. Ralph, and A. G. White, Science **339**, 794 (2013), arXiv:1212.2234.

[25] K. R. Motes, A. Gilchrist, J. P. Dowling, and P. P. Rohde, Physical Review Letters **113**, 10.1103/PhysRevLett.113.120501 (2014), arXiv:1403.4007.

[26] H. Qi, L. G. Helt, D. Su, Z. Vernon, and K. Brádler, arXiv:1812.07015 (2018), arXiv:1812.07015.

[27] K. R. Motes, J. P. Dowling, A. Gilchrist, and P. P. Rohde, Physical Review A - Atomic, Molecular, and Optical Physics **92**, 10.1103/PhysRevA.92.052319 (2015).

[28] A. Deshpande, A. Mehta, T. Vincent, N. Quesada, M. Hinsche, M. Ioannou, L. Madsen, J. Lavoie, H. Qi, J. Eisert, D. Hangleiter, B. Fefferman, and I. Dhand, *Science Advances*, Tech. Rep. 1 (2022) arXiv:2102.12474.

[29] C. Weedbrook, S. Pirandola, R. García-Patrón, N. J. Cerf, T. C. Ralph, J. H. Shapiro, and S. Lloyd, Reviews of Modern Physics **84**, 621 (2012), arXiv:1110.3234.

[30] A. Bouland and S. Aaronson, Physical Review A **89**, 62316 (2014).

[31] A. Sawicki, Quantum Information and Computation **16**, 291 (2016), arXiv:1507.08255.

[32] W. R. Clements, P. C. Humphreys, B. J. Metcalf, W. S. Kolthammer, and I. A. Walsmley, Optica **3**, 1460 (2016), arXiv:1603.08788.

[33] W. R. Clements, *Linear Quantum Optics: Components and Applications*, Ph.D. thesis, University of Oxford (2018).

[34] J. M. Arrazola, T. R. Bromley, and P. Rebentrost, Phys. Rev. A **98**, 12322 (2018).

[35] B. A. Bell, G. S. Thekkadath, R. Ge, X. Cai, and I. A. Walmsley, Optics Express **27**, 35646 (2019), arXiv:1909.02975.

[36] G. S. Thekkadath, B. A. Bell, R. B. Patel, M. S. Kim, and I. A. Walmsley, arXiv:2107.06244 **128**, 10.1103/PhysRevLett.128.023601 (2021), arXiv:2107.06244.

[37] S. Sempere-Llagostera, G. S. Thekkadath, R. B. Patel, W. S. Kolthammer, and I. A. Walmsley, Optics Express **30**, 3138 (2022), arXiv:2111.15308.

[38] N. Killoran, J. Izaac, N. Quesada, V. Bergholm, M. Amy, and C. Weedbrook, Quantum **3**, 129 (2019).

[39] D. Su, R. Israel, K. Sharma, H. Qi, I. Dhand, and K. Brádler, Quantum **5**, 452 (2021), arXiv:2008.06670v4.

[40] J. Lugani, R. J. A. Francis-Jones, J. Boutari, and I. A. Walmsley, Optics Express **28**, 5147 (2020), arXiv:1907.05477.